Final Draft
of the original manuscript:

Khan, S.; Vyshnevskyy, A.; Mosler, J.:
Low cycle lifetime assessment of Al2024 alloy
In: International Journal of Fatigue (2010) Elsevier

DOI: 10.1016/j.ijfatigue.2010.01.014

LOW CYCLE LIFETIME ASSESSMENT OF AL2024 ALLOY

S. Khan[1], A. Vyshnevskyy[2], and J. Mosler[3]

[1,2,3] GKSS Research Centre Geesthacht GmbH,

Max-Planck-Strasse 1, 21502, Geesthacht, Germany

Abstract: The 2024-T351 aluminum alloy is extensively used for fabricating aircraft parts. This alloy shows a relatively low ductility at room temperature and is generally heat treated in various conditions to suit particular applications. The present study experimentally and numerically analyzes the damage mechanism of an Al2024-T351 plate (short transverse direction) subjected to multi-axial stress states. The purpose of this work is to predict the cyclic lifetime of the considered alloy, based on the local approach of damage evolution using continuum damage modeling (CDM). The experimental program involves different kinds of specimens and loading conditions. Monotonic and cyclic tests have been conducted in order to measure the mechanical response and also to perform micromechanical characterization of damage and fracture processes. The cyclic plasticity behavior has been characterized by means of smooth cylindrical specimens. For analyzing the evolution of plastic deformation and damage under multi-axial stress conditions, cyclic loading tests in the low cycle regime have been conducted on different round notched bars. The predictions of the CDM were compared to the experimentally observed mechanical response and to the micromechanical characterization of damage. Emphasis was placed on the prediction of the number of cycles to failure.

1 INTRODUCTION

In contrast to high cycle fatigue (HCF), low cycle fatigue (LCF) is generally characterized by failure in less than 10^4 cycles showing a pronounced plastic mechanical response. These loading conditions can occur in airplane structures during or after unpredictable mechanical impacts, e.g., hard landing, bad weather conditions, operational errors, failure of structural integrity, etc. Today's airplane design is based on numerous tests on specimens of various sizes for the estimation of the residual strength of certain components such as the fuselage. These test programs are time consuming and expensive. The development of predictive models for ductile crack initiation is thus essential for improving structural design and maintenance, and it accelerates the introduction of new materials or assembling methods.

Crack initiation as the result of LCF is a complex process that is influenced by many factors: stress (strain) history, rate of loading, environmental influence, temperature, hold times, etc. In addition to these extrinsic factors, numerous features of the micro-structure of the material undergoing cyclic loading affect crack initiation as well. Low cycle fatigue damage in ductile metals and alloys is usually associated with macroscopically observed plastic deformations. Therefore, it is reasonable to examine stress singularities showing material yielding which leads finally to crack initiation.

In the present paper, the aforementioned physical processes are analyzed by means of continuum damage modeling (CDM). The original version of the CDM approach used here was proposed by Lemaitre (1985). This particular method falls into the range of phenomenological macroscopic material models. Hence, the complexity of the damage processes on the micro-scale is not approximated in detail, but only in an average sense (macroscopically). This is in sharp contrast to the majority of steels which are frequently modeled by means of micro-mechanically sound porous metal plasticity. Unfortunately, the damage mechanisms in highly inhomogeneous and anisotropic aluminum alloys are significantly more complicated that those in steels and hence, porous plasticity theory is not well suited. The CDM approach considered in the present paper approximates the aforementioned physical phenomena by means of plastic deformations and by

damage mechanisms. Conceptually, damage affects the mechanical response through the degradation of the stiffness. Clearly, the application of CDM to the prediction of the mechanical response and the lifetime of complex engineering components and structures subjected to cyclic loading is highly challenging. In this case, the design and the validation of damage evolution laws is required. Particularly, the influence of multi-axial loading on the fatigue life of materials and structures under operational conditions is of utmost importance.

This paper is devoted to the extension and validation of the CDM approach by Lemaitre and Desmorat [1] to high strength aluminum alloys. A very common aluminum Al2024 alloy used for years in the aerospace industry is studied here as a reference. This alloy is preferred because of its good damage tolerance. The work includes both experimental and simulation parts. The experimental program involves different specimen geometries showing various multi-axial stress states. Furthemore, the testing conditions range from monotonic to cycling loading within the LCF regime.

The S-direction (direction perpendicular to the plate) was selected for the current investigation. This is related to previous experimental and modeling activities in our working group [2]. Within the cited work, it was shown, that despite the strong anisotropy of the micro-structure caused by the manufacturing process, the mechanical properties are almost identical in any material direction. The major difference in the mechanical response is the fracture resistance. In this connection, the L- and T-directions are significantly stronger than the S-direction. Furthermore, if loading is applied in S-direction, a fracture surface being perpendicular to the loading direction is observed. As a consequence, the S-direction shows a relatively simple fracture mechanism and thus, it is convenient for further analysis.

The present paper is concerned with the comparison of the results predicted by the aforementioned CDM approach to experiments. Special emphasis is placed on the prediction of the number of cycles to final failure including the locations of crack initiation.

2 MODELING

Axi-symmetric FE models of the specimen geometries were developed using 4-noded standard elements (standard integration). Symmetry conditions are imposed in order to increase computational efficiency. The mesh size in the region of expected failure is of the same order as a representative volume element in metals [1]. The simulations are run by using ABAQUS v6.7 software with Z-Mat as material library. The constitutive behavior of the material was modeled by means of the CDM approach of Desmorat-Lemaitre [3]. This CDM model is based on rate-independent elasto-plasticity (isotropic and kinematic hardening) combined with anisotropic damage evolution (with micro-defect closure effects). Further details can be found in [3]. For the sake of comprehensibility, an overview of the governing equations is presented in the next sections.

2.1 Elasto-plasticity

The model is based on the assumption of additive decomposition of the strains into elastic and plastic parts. More precisely,

$$\overset{\sim}{\dot{\boldsymbol{\sigma}}} = \underline{\mathbf{C}} : \dot{\boldsymbol{\varepsilon}}^{\mathbf{e}} = \underline{\mathbf{C}} : (\dot{\boldsymbol{\varepsilon}} : \dot{\boldsymbol{\varepsilon}}^{\mathrm{p}}), \tag{1}$$

where $\overset{\sim}{\dot{\boldsymbol{\sigma}}}$ - is the effective Cauchy stress tensor (rate) and $\underline{\mathbf{C}}$ - is the 4-th order stiffness tensor.

Yielding is governed by the von Mises-type yield function

$$f = (\widetilde{\boldsymbol{\sigma}} - \mathbf{X})_{\mathrm{eq}} - \mathrm{R} - \sigma_{\mathrm{y}}\,, \tag{2}$$

with $\mathbf{X}$ - being the back stress tensor, R -representing a stress-like internal variable associated with isotropic hardening and σ_y - denoting the (initial) yield stress. Here and henceforth, $(\cdot)_{eq}$ is the equivalent stress measure of von Mises-type.

The evolution of isotropic hardening and that of its kinematic counterpart are governed by an exponential law and an Armstrong-Frederick-type relation, respectively [1, 3]. More precisely,

$$R = R_{\infty}(1 - \exp(-br)), \tag{3}$$

$$\dot{\boldsymbol{X}} = \frac{2}{3}\mathrm{C}\dot{\boldsymbol{\varepsilon}}^{\boldsymbol{p}} - \gamma \boldsymbol{X}\dot{r} \tag{4}$$

Here, R_∞ and b - are parameters defining the isotropic hardening (saturation stress and saturation rate) and r - is a strain-like internal variable (the equivalent plastic strain). Kinematic hardening is described by the material parameters C and γ .

2.2 Damage evolution

For the description of anisotropic damage evolution, a 2-nd order damage tensor $\mathbf{D}$ is introduced. Without going too much into details, the effective stresses are computed from

$$\widetilde{\boldsymbol{\sigma}} = (\mathbf{H}^{\mathbf{p}}\boldsymbol{\sigma}_{+}^{\mathbf{D}}\mathbf{H}^{\mathbf{p}})^{\mathbf{D}} + (\mathbf{H}^{\mathbf{p}}\boldsymbol{\sigma}_{-}^{\mathbf{D}}\mathbf{H}^{\mathbf{p}})^{\mathbf{D}} + \left[\frac{\langle \boldsymbol{\sigma}_{\mathbf{H}} \rangle}{1 - \eta D_{\mathbf{H}}} - \frac{\langle -\boldsymbol{\sigma}_{\mathbf{H}} \rangle}{1 - \eta h_a D_{\mathbf{H}}}\right]\mathbf{I} \tag{5}$$

$$\mathbf{H}_{ij}^{\mathbf{p}} = (\mathbf{1} - \mathbf{D})_{ij}^{-1/2} \text{ and } \mathbf{H}_{ij}^{\mathbf{n}} = (\mathbf{1} - h_a\mathbf{D})_{ij}^{-1/2} \tag{6}$$

where $\boldsymbol{\sigma}_{+}^{\mathbf{D}}$, $\boldsymbol{\sigma}_{-}^{\mathbf{D}}$ - are the positive and the negative part of the deviatoric stresses (based on eigenvalues); $\boldsymbol{\sigma}_{\mathbf{H}}$ - is the hydrostatic stress; $\langle\cdot\rangle$ - are McCauly brackets; η and h_a - are the closure effect and hydrostatic damage sensitivity parameters, respectively.

The damage evolution law is assumed to be a function of the plastic strain rate $\dot{\boldsymbol{\varepsilon}}^{\mathrm{p}}$ and the effective elastic energy density $\overline{Y}$, i.e.,

$$\dot{D}_{ij} = \left(\frac{\overline{Y}}{S}\right)^{s} |\dot{\boldsymbol{\varepsilon}}^{\mathrm{p}}|_{ij} \tag{7}$$

Clearly, $\overline{Y}$ depends implicitly on the stress state and hence, a tri-axiality dependence is included.

An important consideration within the aforementioned damage framework is a threshold value of damage initiation. It is assumed, that damage starts only after the plastic stored energy [4]

$$w_s = \int_0^t R_{\infty}(1 - \exp(-br))\frac{A}{m}r^{(1-m)/m}\dot{r}dt + \frac{3}{4C}\mathbf{X}^2 \tag{8}$$

reaches the value w_D and continues as long as the eigenvalues of the damage tensor $\mathbf{D}$ are less than the critical damage D_c. In Eq. (8), r is the accumulated plastic strain, $\mathbf{X}$ is the back stress

tensor, A,m are parameters defining the plastic stored energy function, and R_∞, b, c are additional parameters describing the cyclic plasticity model (see Eqs. (3)-(4)).

The mechanical response during the strain controlled symmetric cyclic loading can be divided into two stages:

- Initially, a gradual increasing of the stress peaks is observed (see Fig. 1b). It continues till a maximum value. In line with other metallic materials, stabilization of the cyclic mechanical response is observed. At the end of this stage $w_s = w_D$ is fulfilled. The respective number of cycles is denoted as N_D (Fig. 1b).
- During the second stage, the stress peaks start to decrease and mechanical degradation is observed (Fig. 1b). This stage is associated with the initiation and progress of damage ($0 \leq D \leq D_c$). The number of cycles during this stage is denoted as N_E.

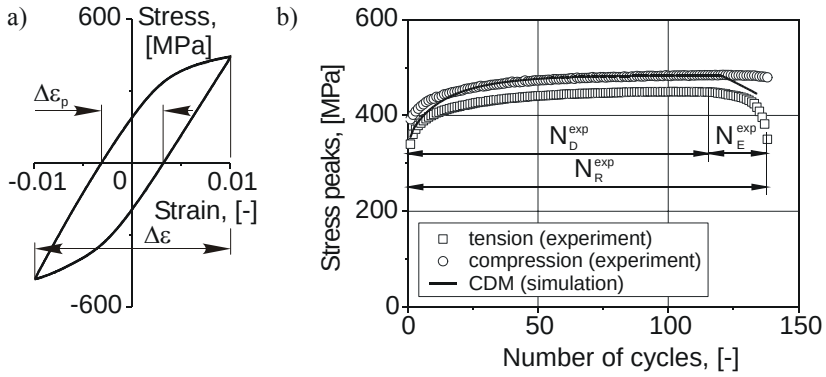

Figure 1: (a) Mechanical hysteresis and (b) Experimental vs. simulated absolute maximum value of tension and compression stresses for a particular strain loading amplitude, DLC-specimen ($\Delta\varepsilon = 0.02$; $\Delta\varepsilon_p = 0.0063$; $N_R^{exp} = 138$).

Beyond, these stages a (meso-) macro-crack in the critical region will be initiated. However, the modeling of crack extension was not considered in the present framework. Summarizing the aforementioned stages, rupture occurs at

$$N_R = N_D + N_E \tag{9}$$

number of cycles (Fig. 1b).

2.3 Modeling with the Coffin-Manson relation

A standard representation of LCF lifetime for uni-axial cyclic loading is based on the relation between plastic strain amplitude $\Delta\varepsilon_p$ and number of cycles to rupture N_R (in logarithmic scale).This results in the so-called Coffin-Manson relation given by

$$N_R = \left(\frac{C_{MC}}{\Delta\varepsilon_p}\right)^{\gamma_{MC}} \tag{10}$$

where C_{MC} and γ_{MC} are material constants [4, 5].

3 EXPERIMENTS

The material under consideration is Al2024-T351. It was supplied in form of a 100 mm thick rolled sheet in the T351 temper (solution heat treated, air-quenched, stress-relieved by cold stretching). The main alloying element in the 2XXX series is copper, while magnesium and manganese are also introduced in order to improve the quenching properties. The material's chemical composition (as specified by the supplier Alcoa Inc., cf. [6]) is given in Table 1 below.

Table 1: Chemical composition limits of Al2024 alloy. Maximum value is given, if range is not shown.

Element	*Si*	*Fe*	*Cu*	*Mn*	*Mg*	*Cr*	*Zn*	*Others, total*	*Al*
Wt.%	0.50	0.50	3.8-4.9	0.30-0.9	1.2-1.8	0.10	0.25	0.15	balance

3.1 Mechanical testing

Two types of specimens were tested (see Fig. 2). A so-called Damage Low Cycle specimen (DLC, smooth round bar) was designed for tension-compression tests showing a stress state close to the uni-axial one (see Fig. 2a). The specimen's dimensions were taken from the ASTM E 606 standard test method, with the following modifications: (i) a shorter gauge length to prevent buckling due to high compression straining; (ii) design of a new gripping for tension-compression testing. Additionally, circumferential Round Notch Bars (RNB) with various radii were designed to achieve a variation of the stress state in the middle cross section of the specimen (see Fig. 2b). The geometry of the RNB specimens was designed similar to that in [7]. All specimens were cut from the same plate of Al2024-T351 in S-direction and they were mechanically treated with a turning machine. The length of the specimens is equal to the thickness of the plate. Hence, the effective measuring length is associated with the mid-plane of the plate under investigation. The surfaces of the specimens were ground and mechanically polished in the direction of loading. The final polishing was performed with a diamond paste showing 1μm grains.

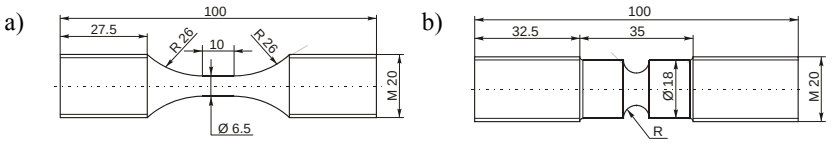

Figure 2: Specimen geometries: (a) DLC-specimen; (b) RNB specimen with circumferential notches $R = 10mm$ and $R = 2mm$.

The entire experiments were conducted on a $160kN$ servo-hydraulic testing machine Schenck H160. Specially designed gripping of the testing setup and clamping threads of the specimens allow for tension-compression reversal loading. The cyclic tests in all cases were performed displacement-controlled. The displacement was measured using an extensometer attached to the working distances in the case of the DLC-specimen in Fig. 3a. For the RNB-specimen in Fig. 3b and 3c, the extensometer was attached to the specially manufactured grooves. A symmetric cycle ($R = -1$) based on a triangular wave shape was imposed with various displacement amplitudes Δl. The time period was not varied ($T = 100s$). All tests were conducted until complete failure

(separation of the specimen into two parts). Time-force-displacement responses during the tests were recorded with a digital acquisition device.

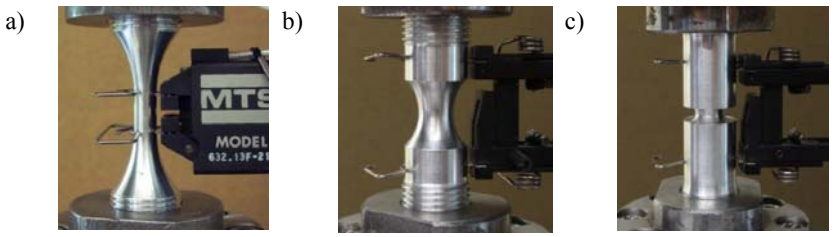

Figure 3: Attachment of the strain gage: (a) DLC-specimen; (b, c) RNB specimens with circumferential notches $R = 10mm$ and $R = 2mm$.

Within the present paper, focus is on the application of the CDM approach to the analysis of LCF in Al2024. Thus, it is not intended to conduct as many experiments as necessary for certain statistics. Nevertheless, some of the experiments were repeated with identical loading conditions to check the reproducibility of the mechanical response. For the modeling proposes only selected experiments have been used. The whole experiments are summarized in Tab. 2.

Table 2: Matrix of LCF experiments.

Specimen	Notch. mm	Gage length, mm	Range of Δl , mm	Number of specimens
DLC	-	10 mm	0.01-0.4	14
RNB	2mm	25 mm	0.025-0.1	10
RNB	10mm	25 mm	0.075-0.1875	6

3.2 Micro-structure investigations

In order to successfully predict the lifetime of a material, it is important to understand its damage evolution. Damage in Al-alloys usually nucleates at large and brittle intermetallic particles or coarse precipitates, and sometimes also at smaller particles such as dispersoids or precipitates [8-10]. In the specific case of fracture in high strength Al-alloys, the intergranular damage is induced by growth of voids around coarsened precipitates in ductile Precipitate Free Zones (PFZ) [11]. Optical microscopy (OM), scanning electron microscopy (SEM) and X-ray micro-tomography (XTM) have been used in our working group in the past to obtain quantitative information about micro-structural characteristics [12]. For fracture and LCF damage, the analysis of big intermetallic particles (equivalent diameter $23.5 \pm 16.7\ \mu m$) aligned in a network-like structure (clusters or Precipitate Free Bands (PFB)) which separate the matrix into domains is of utmost importance. The majority of them are Al_2CuMg particles appearing in SEM pictures (BSD mode) in Fig. 5 a and Fig. 5b in white color. According to XTM investigations, the domains have a disc-like shape, with the S-direction as the shortest axis and almost identical dimensions in L- and T-directions. This microstructure results in higher damage rates in the PFB, if the material is loaded in S-direction. When damage evolves further, the most probable macroscopic crack is perpendicular to the loading direction with “shearing jumps” between parallel PFBs [2]. To systematically characterize fatigue fracture, fracture surfaces corresponding to monotonic loading were compared to their cyclic counterparts. 2D and 3D snapshots of the micro-structure have been extracted.

For monotonous loading, the fracture surface shows a dense dimple structure, which is characteristic of ductile failure (Fig. 4a). However, the picture provides only two-dimensional information (the depth is missing). More details about the depth will be given in the subsequent paragraphs. Some multiple cracks are also present at the surface of the notch. Slight necking in the notch root is observed.

a) b)

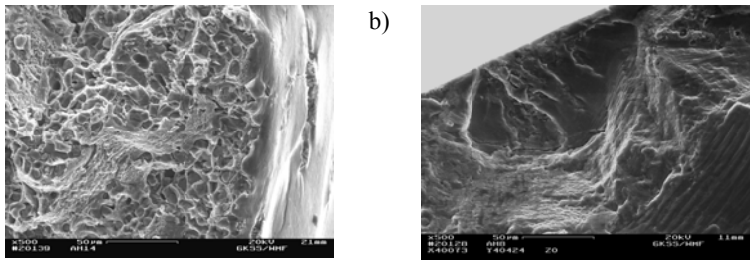

Figure 4: SEM of fracture surface close to the notch root of (a) monotonically loaded specimen, and (b) cyclically loaded specimen (703 cycles)

In cyclic loading (Fig. 4b), large single "craters" (due to particle embedding) appear close to or directly at the edge of the fracture surface. This is a strong indicator for failure originating from the surface. Fatigue lines are highly visible around the single "craters". By way of contrast, in the monotonic case, the appearance of multiple broken particles just under the fractured surface in the middle of specimen (Fig. 5a) is evident. This is not the case in the region close to the notch root (Fig. 5b). Hence, the crack starts in the middle of the specimen and propagates to the surface. The specimens in Figs. 5a,b have been cut und polished in the longitudinal direction.

a) b)

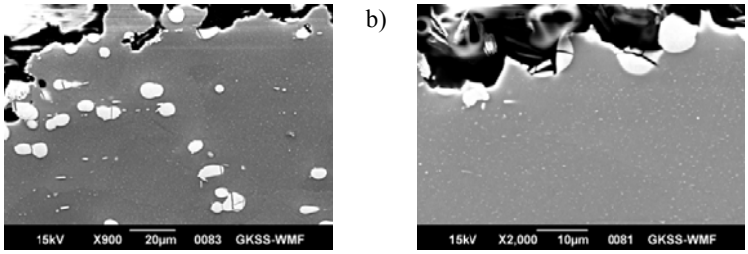

Figure 5: SEM of longitudinal micro-sections close to the fracture surface of the monotonically loaded RNB specimen (a) middle of the specimen, (b) region close to the notch root

Imaging software (Alicona) combined with SEM was used to study the 3D shape of the fracture surfaces. In Fig. 6a, it can be seen that the fracture initiates at various height levels, creating an uneven structure. This kind of ductile damage occurs at various stages within the material's layers. Finally, the scattered micro-cracks coalesce and form a macro-crack. The bright planes in Fig. 6a represent the shearing ductile fracture. Accordingly, so-called shear lips (smoothened dimples due to shear deformation) are observable (instead of dimple structures). In the LCF-regime (Fig. 6b), the mechanisms change to mixed-mode failure. Consequently, uneven ductile failure areas, fatigue lines and shear lips are visible. Failure starts within clusters of particles. Subsequently, with increasing accumulation of plastic strain, dense dimple structures appear. Finally, the distributed damaged zones connect to each other due to ductile cracks propagation and coalescence (fatigue lines). However, shearing ductile fracture as observed for monotonic loading, can be seen as well.

a) b)

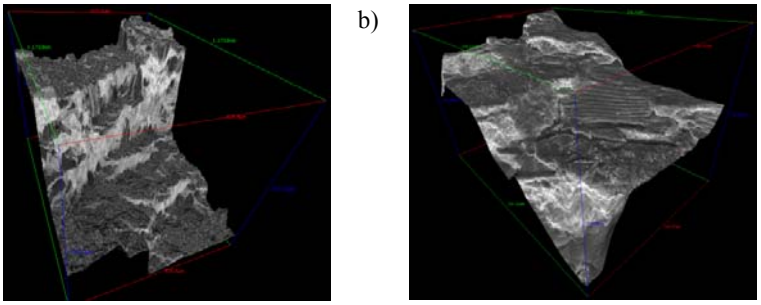

Figure 6: 3D re-constructed fractured surface (a) monotonous loading and (b) cyclic loading

Evidently, a complete understanding of the aforementioned mechanisms requires particularly a careful analysis of damage evolution at the micro-scale. Consequently, non-destructive micro-structural techniques such as synchrotron X-ray micro-tomography have also to be applied. During the last 10 years, significant progress has been made in terms of resolution. More precisely, the spatial resolution is now close to that of an optical microscope (*2-3 μm*). In the field of damage/fracture characterization, micro-tomography has been used for visualizing cracks in metals also for Al-alloys [13-16].

a) b) c)

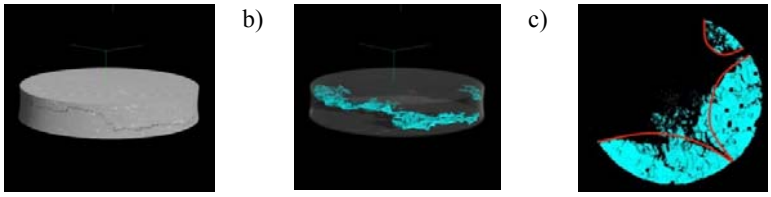

Figure 7: Section of reconstructed XTM 3D-image: (a) as a full solid, (b) as a semi visible volume with cracks, and (c) projection of the crack front on the plane perpendicular to the axis of specimen

In Fig. 7, results obtained from XTM are shown. The geometry of the notch specimen is slightly modified to adjust the cross section size to the XTM penetration capability. E.g., the inner diameter is *4mm* and the notch radius is *4mm* as well. This is geometrically equivalent to the *10mm* notch geometry used before. With the help of SEM and XTM micrographs, the results of the CDM reported in the next sections can be proven (particularly, the evolution of damage), cf. [17]. So far, the XTM measurements have been performed after loading the specimen. In the future, true in-situ investigations will be conducted. By doing so, the mechanisms of damage evolution can be investigated at a fine temporal and spatial resolution.

4 SIMULATION RESULTS

4.1 Material parameters of the plasticity model

For the simulation of the cyclic mechanical response, a combined isotropic-kinematic hardening plasticity model is used. Since no damage occurs within the first N_D^{exp} cycles (see Fig. 1a), the material behavior is purely elasto-plastic (without damage). The material parameters were adjusted using experimental cyclic stress-strain curves of DLC-specimens for $\Delta\varepsilon = 0.02$. The resulting material parameters are summarized in Table 3.

Table 3: Elasto-plastic parameters model

Elasticity		***Plasticity***				
$E\ [MPa]$	υ	$\sigma_y[MPa]$	$R_\infty[MPa]$	b	γ	$C[MPa]$
$7{\cdot}10^5$	0.3	284	150	4	80	$1.7{\cdot}10^4$

Since a von Mises yield function is adopted, the tension-compression asymmetry is not captured. However, this can easily be improved by using a more realistic yield function.

4.2 Material parameters for the damage model

The material parameters are calibrated starting with those for the evolution and the threshold value of the stored plastic energy function, cf. Eq. (8). For that purpose, an analytical method related to the underlying model is frequently applied, cf. [18]. Within this method it is assumed, that the isotropic hardening function reaches saturation prior to damage initiation. This is a common observation in ductile steels. Unfortunately, Al2024-T351 does not exhibit such a stabilization and thus other methods have to be used.

In the present work, the objective function [19]

$$\{A, m, w_D\}^* = \underset{\{A,m,w_D\}\in R_+^3}{\operatorname{argmin}} \left(\sum_{i=1}^{M} \left(\log {N_D^{exp}}_i - \log {N_D^{sim}}_i(A, m, w_D) \right) \right) \tag{11}$$

is minimized, where ${N_D^{exp}}_i$ and ${N_D^{sim}}_i$ are the experimentally observed cycles before damage initiation and the numerically computed counterparts (see Fig. 1b). M is the number of experiments (with different loading amplitudes). The problem is solved by implementing an algorithm in MATLAB. The whole set of material parameters is summarized in Tab. 4.

Table 4: Parameters of the model governing the evolution and the threshold values of the stored plastic energy and the damage evolution

Stored plastic energy			***Damage***				
m	A	$w_D\ [MJ/m^3]$	$S\ [MJ/m^3]$	s	η	h_a	D_c
3.9	0.0113	0.897	1.3	1.0	2.8	0	0.1

The choice of the damage parameters is motivated by the macroscopic material behavior. In several experiments with DLC-specimens no degradation of the mechanical properties was observed. The decreasing of stresses showed a rather abrupt or "quasi-brittle" character. A fast evolution of damage and a small value of critical damage D_c suit such a material behavior well. The parameters for abrupt fracture and gradual degradation of the material behavior (e.g. Fig. 1b) are given in Table 4. The damage parameter was calibrated, without an optimization technique.

4.3 Simulation of fatigue lifetime of DLC-specimens

Fig. 8 shows the results of FEM simulations performed on one single 3D finite element with the set of CDM-parameters taken from Tab. 3 and 4. For the sake of comparison, experimental

results, together with the Coffin-Manson model, are shown as well. The parameters of the Coffin-Manson model are $C_{MC} = 0.196$ and $\gamma_{MC} = 1.4$.

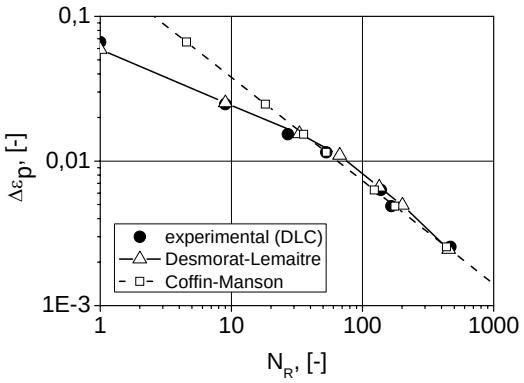

Figure 8: Experimental vs. simulated fatigue response of DLC-specimens

According to Fig. 8, the CDM fits almost perfectly the experimental data. For all loading amplitudes the agreement between the experimental observations and the numerically predicted response is remarkable. Furthermore, the predictions of the Coffin-Manson model are very good as well. Only if failure occurs in less than 30 cycles, this purely empirical model cannot be applied anymore. However, it bears emphasis that although both models lead to realistic results for more than 30 loading cycles, only the CDM approach is based on fundamental physical principles such as the second law of thermodynamics and equally importantly, only the CDM model can also be applied to more complex engineering problems, i.e., it is structure independent.

4.4 Lifetime prediction

An example of a typical force-displacement and force-time response of the notched specimen is presented in Fig. 9.

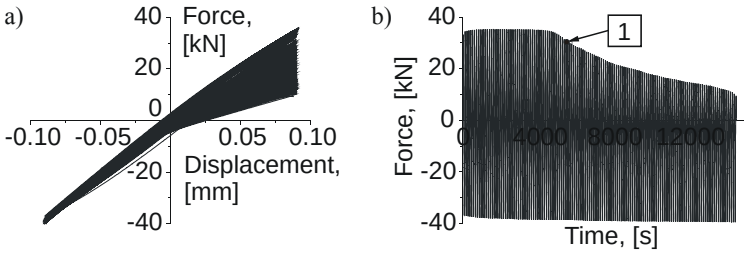

Figure 9: (a) Force-displacement and (b) Force-time responses of the notched specimen ($2\,mm$ notch, $\Delta l = 0.02\,mm$). Point 1 indicates the formation of a crack at the surface of the specimen

The curves are similar to those of the DLC-specimen. The two stages of material hardening and degradation as mentioned formerly are evident (see Fig. 1b). In contrast to the DLC-specimens, the second stage is significantly longer. This will be explained in what follows.

The results of FE simulations (not included in the present article) reveal that with decrease of loading amplitude and increase of notch curvature the plastic deformations will be localized in the notch root. At the same time, the remaining volume of the specimen deforms purely elastically. If loading is further increased, this leads to crack propagation in an almost fully elastic specimen. Thus, from a structural point of view, this problem is mostly related to fracture mechanics. Evidently, the aforementioned CDM approach is not well suited for the modeling of such a process. Therefore, crack initiation (Point 1 in Fig. 9b) is chosen as the state defining N_R, see Eq. (9).

The results of the FEM simulation are compared to those of the experiments in Fig. 10.

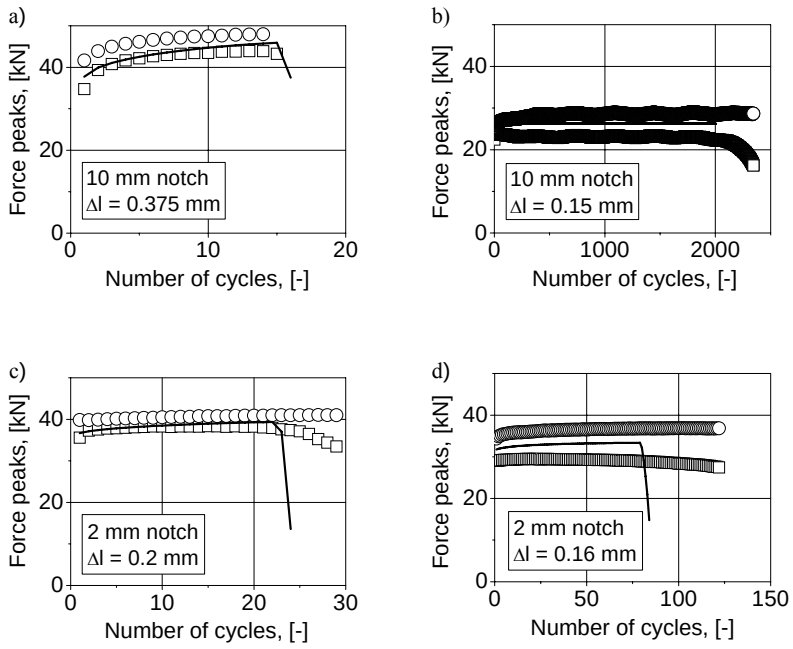

Figure 10: Experimental (□ - tension, ○ - compression) vs. simulated (— CDM) force peaks. The simulation presented in (b) was stopped due to saturation of the stored plastic energy function (2000 cycles)

The results, presented in Fig. 10, show the mechanical response for extreme combinations of notch geometries and loading amplitudes. The best prediction was achieved for the 10 mm notch and the highest loading amplitude (Fig. 10a). Although the numerical results are very promising, some differences compared to the experimental data can be seen. One possible reason for this is the calibration method, i.e., for calibrating the material parameters, the onset of crack initiation is required (see point 1, Fig. 9b). However, this point is not defined precisely by the conducted experiments (certain assumptions were necessary). Additionally, further investigations concerning the limits of the model (small strain amplitude, high stress tri-axiality) are required.

By analyzing Fig. 10b, the range of applicability of the CDM approach can be estimated. More precisely, the amplitude of the imposed displacement is so small, that after stabilization of the hysteresis due to saturation of isotropic hardening, the hysteresis width is very small. Accordingly, the rate of further plastic strains will be very small as well. As a consequence, the stored plastic energy increases only very slowly and hence, damage initiation will not occur within a reasonable number of cycles ($w_s < w_D$).

Table 5: Comparison of the simulation results to the experimental data for the notched specimens. * - stopped after 2000 cycles

Notch radius, [mm]	$\Delta l,[mm]$	$N_D^{\exp}$	N_D^{sim}	$N_R^{\exp}$	N_R^{sim}
10	0.375	14	15	15	16
10	0.200	204	378	431	383
10	0.150	2010	- *	2345	- *
2	0.20	19	22	26	24
2	0.18	36	43	55	45
2	0.16	63	79	122	84

The comparison of the predicted fatigue lifetime is summarized in Table 5.

From Table 5 the relative error in the predicted lifetime can be computed. Defining the error as

$$\delta = \frac{\log N_R^{exp} - \log N_R^{sim}}{\log N_R^{exp}} . 100\% \tag{12}$$

it is less that 7.8%.

Figure 11 shows the error involved between experiments and the FEA (finite element analysis) with aforementioned Lemaitre unified damage model.

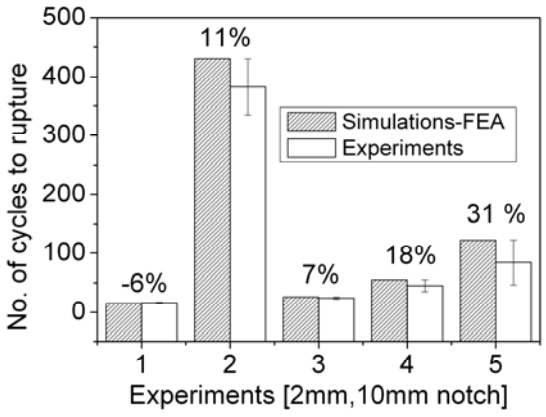

Figure 11: Bar graph showing the error, experiments and FEA.

Two damage distributions in loading direction at the rupture time point $N - N_R$ are shown in Fig. 12.

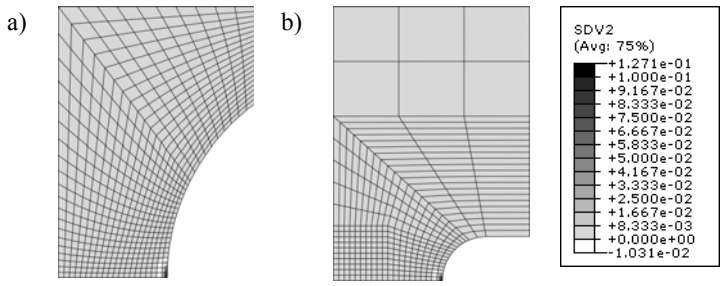

Figure 12: Distribution of damage in loading direction at the rupture time point ($N = N_R$). (a) Notch radius $10mm, N_R = 431$; (b) Notch radius $2mm, N_R = 55$.

The region of crack initiation is predicted very accurately. It is in excellent agreement with similar investigations for ductile steels [7]. The major difference as compared to the distribution of damage in steel is the pronounced localization of damage in the notch root.

5 CONCLUSIONS

Low cyclic fatigue behavior of Al2024-T351 alloy was investigated using mechanical testing, micromechanical characterization of fracture surfaces and X-ray micro tomography for various specimen geometries and loading regimes. The predictive capability of the Desmorat-Lemaitre CDM model [1] was analyzed for high load reversals under various stress states and lifetimes.

For simple stress states, the results predicted by the CDM approach have shown very good agreement with experimental data. In contrast to the Coffin-Manson model, the CDM approach can even be applied to the analysis of material failure in less than 30 cycles. However and even more importantly, the CDM approach is, in contrast to the Coffin-Manson model, based on fundamental physical principles such as the second law of thermodynamics and hence, it can also be applied to more complex engineering problems, i.e., it is structure independent. This was demonstrated by analyzing more complex geometries. Again, the lifetime prediction was in good agreement with experiments (the error is less than 7.8%). It was shown, that with an increased tri-axiality (curvature of notch) and an increased number of cycles to rupture, the initiation of damage will be overestimated and the number of cycles to rupture will be underestimated. Further investigations in this direction are thus necessary for lifetime predictions of complex structural components.

ACKNOWLEDGMENTS

The authors gratefully acknowledge D. Steglich, W. Brocks, R. Desmorat, J. Besson, J. Herrens for useful advises, J. Knaack for mechanical testing, P. Fischer for metallography and V. Ventzke for SEM-analysis.

REFERENCES

[1] J. Lemaitre, J.-L. Chaboche, Mechanics of solid materials, Cambridge University Press, New York, 1990.

[2] D. Steglich, W. Brocks, J. Heerens, T. Pardoen, Anisotropic ductile fracture of Al 2024 alloys, Eng. Fract. Mech. 75, (2008), 3692-3706.

[3] J. Lemaitre, R. Desmorat, Engineering Damage Mechanics, Springer, Heidelberg, 2005.

[4] A. Chrysochoos, Dissipation et blocage d'energie lors d'un ecrouissage en traction simple, Thèse d'état de l'université, Paris, 1987.

[5] L.F. Coffin, Stress and Reliability in Design, J. Vibration, Acoustics, Trans. ASME. 108 (1986) 241-248.

[6] http://www.alcoa.com/mill_products/catalog/pdf/ alloy2024techsheet.pdf

[7] A. Pirondi, N. Bonora, D. Steglich, W. Brocks, D. Hellmann, Simulation of failure under cyclic plastic loading by damage models, Int. J. Plast. 22, (2006) 2146-2170.

[8] T. Pardoen, A. Pineau, Failure mechanisms of metals, in: Comprehensive structural integrity encyclopedia, vol. 2., Elsevier, Amsterdam, 2007. [Chapter 6].

[9] D. Lassance, D. Fabrègue, F. Delannay, T. Pardoen, Micromechanics of room and high temperature fracture in 6xxx Al alloys, Prog. Mater. Sci. 52 (2007) 62-129.

[10] G.G. Garrett, J.F. Knott, The influence of compositional and microstructural variations on the mechanisms of static fracture in aluminium alloys, Metall. Trans. 9A (1978) 1187-1201.

[11] M. de Hass, J.Th.M. De Hosson, Grain boundary segregation and precipitation in aluminum alloys, Scripta Mater. 44 (2001) 281-286.

[12] G. Quan, J. Heerens, W. Brocks, Distribution characteristics of constituent particles in thick plate of 2024 Al-351, Prakt. Metallogr. 41 (2004) 304-313.

[13] A. Guvenilir, T. M. Breunig, J. H. Kinney, S. R. Stock, Direct observation of crack opening as a function of applied load in the interior of a notched tensile sample of Al---Li 2090, Acta Mater. 45(5), (1997) 1977-1987.

[14] A. Guvenilir, T.M. Breunig, J.H. Kinney and S.R. Stock, New direct observations of crack closure processes in Al–Li 2090 T8E41, Philos. Trans. R. Soc. London 357, (1999), 2755–2775.

[15] K. Khor, J.Y. Buffière, W. Ludwig, I. Sinclair, High resolution X-ray tomography of micromechanims of fatigue crack closure, Scripta Mater. 55(1), (2006) 47-50.

[16] H. Toda, I. Sinclair, J. -Y. Buffière, E. Maire, T. Connolley, M. Joyce, K. H. Khor, P. Gregson, Assessment of the fatigue crack closure phenomenon in damage-tolerant aluminium alloy by in-situ high-resolution synchrotron X-ray microtomography, Philos. Mag. 21, (2003) 2429-2448.

[17] R. Braun, D. Steglich, F. Beckmann, Damage mechanism and LCF crack extension in Al2024, DESY Annual Report, (2006) 497-498.

[18] S. Otin, Lois d'endommagement incrementales isotrope/ anisotropies pour applications thermomecaniques complexes, Thèse d'état de l'ecole normale superieure de Cachan, Cachan, 2007.

[19] A. Vyshnevskyy, S. Khan, J. Mosler, An investigation on low cycle lifetime of Al2024 alloy, J. Key Engng. Mat. 417-418, (2009) 289-292.